DESIGN OF A NONSTANDARD FLEXIBLE GRAPHITE COMPOSITE SEALING GASKET FOR PRESSURE OPERATION

Yulong Shu[1], Wentao Dong[1*], Hong Zhang[2], Shaohan Lv[1], Yingshuo Wang[1], Jiahui Li[1]

[1].Department of Petroleum and Natural Gas Engineering, Liaoning Petrochemical University, Liaoning, China
[2] CNPC Engineering Technology R&D Company Limited, Beijing, China

ARTICLE INFO

***Article history*:**
Received: 5. 5. 2025.
Received in revised form: 15. 7. 2025.
Accepted: 16. 7. 2025.

Keywords:
nonstandard graphite gasket
triangular convex array tooth structure
orthogonal test
regression equation
hydrostatic pressure experiment

DOI: 10.30765/er.2905

Abstract:

To address the leakage failure of the nonstandard sealing gasket frame–graphite interface of coupling inspection equipment under high pressure, a multilevel nesting seal structure based on a composite flexible graphite layer of periodic triangular teeth is proposed. Using the L_{27} $(3)^4$ orthogonal test method and Pyron data fitting, a quantitative regression model of structural parameters was established to analyze the influences of the skeleton thickness, arc radius, wave tooth depth and wave tooth pitch on gasket deformation. The results show that the skeleton thickness has the greatest influence, followed by the wave tooth pitch, and the wave tooth depth and arc radius have the least influence. The nonlinear deformation regression model is optimized by considering the interaction of key structures, and its effectiveness is verified via analysis of variance. The deformation of the gasket is 0.54 mm through ANSYS simulation, and the correctness of the model is verified. The workbench simulation shows that the compression rate of the optimized gasket reaches 24.0%, and the rebound rate reaches 87.8%, meeting the national standard. The hydrostatic test results indicate that the sealing performance of the proposed structure is better than that of the traditional gasket under a pressure of 31.5 MPa, meeting the working condition requirements. This study provides a reference for high-pressure seals and special flange designs.

1 Introduction

In the oil and gas industry, owing to the complexity of the production conditions and the multiparameter coupling of the process flow, the sealing performance of the flange–gasket connection structure has become one of the core elements that restricts the safety level of the engineering system. The failure mechanism directly increases the risk of medium leakage and affects the reliability of the device [1]. With the coordinated development of materials science and sealing technology, flexible high-strength graphite gaskets can effectively adapt to complex sealing surfaces and achieve stable sealing due to their excellent compression resilience, high mechanical strength, excellent high-temperature resistance, and chemical corrosion resistance, and they are widely used in the field of sealing under extreme conditions [2]. Yang Dongjun used ABAQUS software to conduct in-depth research on different wave tooth shapes and discussed the tooth depth, tooth thickness, and load–deformation characteristics of trapezoidal wave tooth gaskets, corrugated wave tooth gaskets, circular arc wave tooth gaskets, and V-shaped wave tooth gaskets. The corrugated metal skeleton has better compression and resilience performance [3]. With respect to the sealing failure of flexible graphite metal corrugated composite gaskets for valves under high-temperature and high-pressure conditions, Liu Jie effectively solved short-term sealing failure and verified engineering applicability in a 260 °C high-temperature environment by optimizing the gasket structure and high-temperature bonding process [4]. Chen Qing used the orthogonal analysis method to analyze and calculate that a W-shaped flexible graphite metal winding gasket with a steel strip angle of 102.84°, a winding tension force of 12 N, and a winding pressure of

* Corresponding author
E-mail address: 2497910426@qq.com

0.3 MPa had the best rebound rate [5]. However, the problems of insufficient adaptability of existing sealing gaskets and sealing failure of specific tooth structures under dynamic loading have not been effectively solved. In the special-shaped side door seal of the shell of the coupling detection equipment with pressure operation, the sealing gasket is prone to percolation leakage at the skeleton–graphite interface under high-pressure loading. In this work, a new sealing gasket skeleton structure is designed. Based on multiple linear regression theory, by constructing a nonlinear contact finite element model and using the orthogonal method, the coupling mechanism of the geometric parameters of the skeleton structure on its strength is systematically analyzed, and compression resilience simulations and hydrostatic pressure experiments are carried out to verify the feasibility of its engineering application.

2 Sealing Theory Research

The gasket seal is a type of contact seal, which is dominated by the mechanical behavior of the contact interface and achieves the purpose of the fluid seal through the medium barrier and barrier construction. The control of pretightening pressure, the utilization of material nonlinear deformation, the optimized design of surface contact, and the effective suppression of environmental coupling by the sealing gasket realize the directional transformation from macroscopic mechanical parameters to microscopic sealing performance. Macroscopically, the sealing interface pretightening stress is greater than the fluid pressure to achieve sealing, and the greater the pretightening stress is, the greater the sealing effect. However, owing to the interaction between the surface topography parameters and the preload, a greater preload intensifies the sealing gasket creep phenomenon, resulting in accelerated sealing failure and leakage.

2.1 Sealing Mechanism

The microstructure of a material determines its sealing performance, wear mechanism, and environmental lubrication effect. By optimizing the material matching and interface design, the reliability of the seal can be significantly improved, which provides theoretical guidance for engineering seal systems [6]. The micropore closure effect and elastic recovery characteristics of highly elastic materials in high-pressure environments endow gaskets with the adaptive adjustment ability of expansion-contraction behavior caused by dynamic pressure fluctuations.

In the initial sealing stage, the gasket is subjected to elastic deformation caused by the bolt preload transmitted by the flange surface (as shown in Fig1. Initial Seal). When the pretightening force reaches the critical threshold, the gasket compression deformation mechanism can effectively fill the geometric defects of the sealing interface and seal the leakage path, forming a multichannel interface coupling seal layer of metal and flexible material. The average pretightening pressure value generated in this process can be calculated via Formula (1):

$$\sigma_{go} = \frac{F_0}{A_g} \tag{1}$$

In the equations above:

σ_{go} —average preload pressure, MPa;

F_0 —preload, MPa;

A_g —gasket compression area, mm^2.

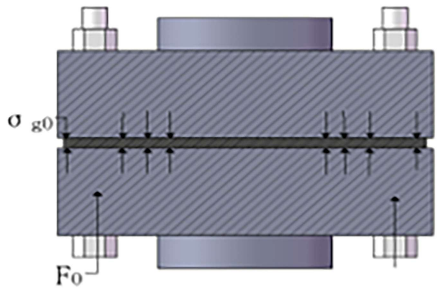

Figure 1. Initial Seal.

In the working sealing stage, the sealing structure is subjected to fluid pressure to produce flange separation, and the sealing gasket dynamically compensates for the increase in the interface gap by releasing elastic strain energy, as shown in Fig2. Working Seal. At the same time, it overcomes the sealing stress attenuation caused by the creep–relaxation coupling effect in long-term work. The average pressing stress required to maintain dynamic sealing performance in this stage can be calculated via Formula (2):

$$\sigma_{\mathrm{g}}=\frac{F_0-\pi P_i r_e^{\ 2}}{A_g} \tag{2}$$

In the equations above:

σ_g —average compression stress, MPa;

P_i —pressure in the pipe, MPa;

r_e —gasket effective contact radius, mm.

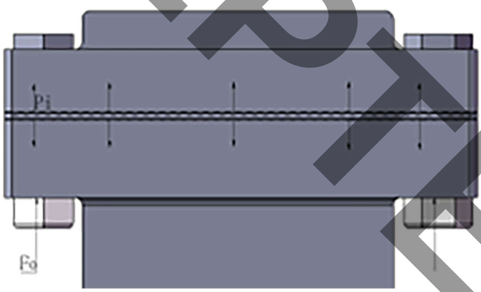

Figure 2. Working Seal.

2.2 Mechanism of Gasket Leakage

Under dynamic service conditions, the flange–gasket system undergoes stress redistribution, and the alternating load causes nonuniform evolution of the contact stress field, resulting in the generation of cyclic elastoplastic deformation in the microscopic contact area and the generation of leakage paths [7]. The gasket sealing interface is essentially a micronano-scale contact system with fractal characteristics, and its surface morphology is composed of randomly distributed asperity contact points and submicron pore networks. Limited by the limitations of modern manufacturing processes, there must be percolation channels at the sealing interface. When the operating pressure difference exceeds the critical value of the capillary force, the interface percolation mechanism is activated, resulting in leakage [8], [9]. On the basis of the difference in the formation mechanism of the leakage path, the gasket leakage mode is composed mainly of interface leakage and penetration leakage, and the leakage mechanism is shown in Fig3. Sealing Leak.

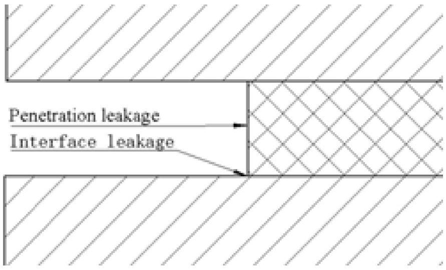

Figure 3. Sealing Leak.

Interface leakage is the dominant mode of sealing failure. Owing to various uneven gaps on the flange surface caused by machining, a percolation channel is formed at the contact interface. Driven by the pressure gradient, the medium migrates radially along the contact interface [10]. Its leakage Q_i can be calculated via Formula (3):

$$Q_i = \frac{\pi h^3 p_i}{6\mu \ln(\frac{r_1}{r_2})} \tag{3}$$

In the equations above:

Q_i —interface leakage, ml·min^{-1};

h —gasket thickness, mm;

p_i —internal and external pressure difference, pa;

μ —fluid viscosity, pa·s;

r_1 —gasket outer diameter, mm;

r_2 —gasket inner diameter, mm.

The seepage leakage is derived from the cross-scale mass transfer behavior inside the porous medium. The mechanism can be constructed on the basis of the capillary beam model, which is characterized by the percolation characteristics of the fluid in the material pore network driven by the pressure difference. Compared with interface leakage, it has the characteristics of a cumulative effect and concealment. Seepage leakage Q_p is restricted by the physical properties of the medium and the structure and material of the gasket, as shown in Formula (4):

$$Q_p = \frac{\pi h^4 p_i}{128\mu L} \tag{4}$$

In the equations above:

Q_p —permeability leakage, ml·min^{-1};

L —gasket effective radius, mm.

2.3 Evaluation and Analysis

The flexible graphite composite gasket is integrated with the expanded graphite compression process through the metal skeleton. Compared with traditional graphite materials, it has low strength, low stiffness, and high elastic dissipation characteristics. The metal skeleton provides the necessary elastic and structural support for the gasket, and the embedded graphite layer ensures the tight fit a leakage control of the sealing surface through its high-density characteristics [11]-[13]. Under the action of bolt preloading, flexible graphite undergoes plastic flow and microstructure rearrangement under the constraint of metal skeleton grooves to form a multiple-sealing mechanism [14]. Through the filling of microgap on the contact surface and the change in elastic energy under dynamic loading, the interface contact strengthening caused by this deformation can significantly improve the sealing effect. Combining the elastic recovery characteristics of the metal skeleton with the compressibility of the flexible graphite phase, the dynamic sealing stability can still be maintained in a pressure fluctuation environment.

The compression rebound characteristic is an important index for measuring the mechanical properties of a gasket. The compression ratio is an index that describes the degree of thickness change of a material under stress, reflecting the ability of the gasket to compress and maintain the sealing effect when subjected to external pressure. According to the load applied on the flange, the contact area between the flange and the gasket, and the axial deformation of the gasket, the compression rebound rate of the gasket can be calculated [15]. A higher compression ratio means that the gasket can better fit with the joint surface when it is under pressure, fill a small gap, and enhance the sealing performance. The calculation formula of the compression ratio is shown in Formula 5:

$$\text{compression ratio}(\%) = \frac{\Delta T_1}{T_1} \times 100 \tag{5}$$

In the equations above:

ΔT_1 —Style compression under total load, mm;

T_1 —pattern under initial load, mm.

After the initial pretightening of the flange sealing structure, owing to the pressure of the operating medium, the applied load, and the thermal load, the flange sealing surface is relatively separated, and the gasket must undergo sufficient elastic deformation to compensate [16]. The gasket thickness recovery reflects the resilience of the gasket and characterizes the compensation ability after separation of the sealing surface. A gasket with good resilience can maintain an effective sealing effect and reduce the risk of fluid leakage. Its formula is as shown in Formula 6:

$$\text{rebound ratio}(\%) = \frac{\Delta T_1 - \Delta T_2}{\Delta T_1} \times 100 \tag{6}$$

In the equations above:

ΔT_2 —The amount of unrecovered compression of the pattern under return to the initial load, mm.

The reliability of the sealing system is restricted by the multiple attributes of gaskets. It is necessary to construct a sealing system adapted to the environment through the collaborative implementation of material characteristic screening, structural design, and leakage path suppression to realize the comprehensive prevention and control of leakage risk.

3 Sealing Gasket Design

3.1 Size structure

The bolt–gasket–flange connection system is transmitted mainly to the sealing gasket through the upper and lower flanges by the bolt pretightening force so that the gasket is axially deformed to compensate for the failure of the flange surface. On the basis of the needs of the pressure operation coupling detector, a rectangular matrix and an embedded symmetrical sawtooth structure are used to increase the number of sealing layers to reduce leakage. The seal gasket structure is shown in Fig4. Gasket Structure Size. The size is 310.0 mm × 190.0 mm × 5.0 mm, the inner rectangular size is 180.0 mm × 105.0 mm × 5.0 mm, and the nut diameter is 25.0 mm.

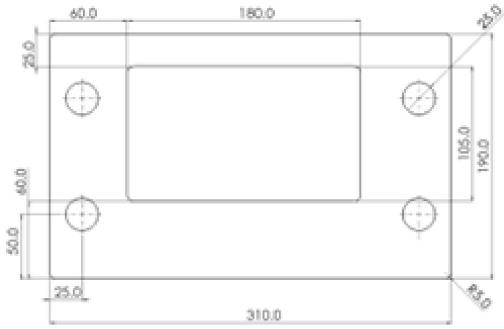

Figure 4. Gasket Structure Size.

In this study, flexible graphite was used as the sealing layer, and TC4 titanium alloy was used as the support skeleton to construct the composite sealing gasket. To overcome the excessive yield strength of the TC4 titanium alloy, the corrugated structure was selected as the skeleton structure [17]. The skeleton thickness, arc radius, wave tooth depth, and wave tooth spacing of the corrugated skeleton are the main parameters that directly affect the structural strength of the gasket and the indentation of the flexible graphite and indirectly affect the gasket sealing effect. The structural parameters of the skeleton need to be considered comprehensively to ensure the effectiveness and reliability of the gasket.

To address the problem of percolation leakage at the skeleton–graphite interface of a nonstandard sealing gasket under high-pressure conditions, through microscopic observation and field analysis, the traditional wave tooth structure easily forms a percolation channel because of insufficient sealing layers under high-pressure alternating loads, resulting in excessive seepage leakage at the contact between the graphite layer and the metal skeleton. Therefore, constructing a periodic equilateral triangular convex array at the wave tooth spacing is innovatively proposed, as shown in Fig5.Skeleton structure. A multistage nested sealing interface is constructed to overcome seepage leakage, and the skeleton structure is optimized on this basis.

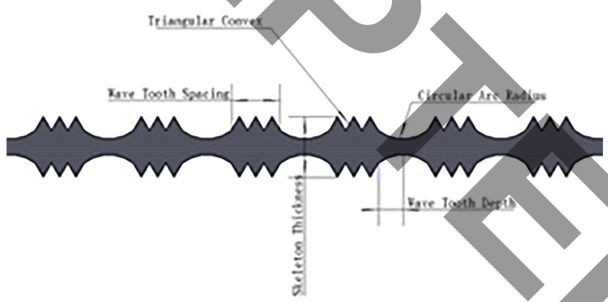

Figure 5. Skeleton Structure.

3.2 Model Calculation

On the basis of the ANSYS Workbench statics module, a parametric finite element model of the sealing gasket is constructed, and a multivariate linear regression equation is established by extracting the shape variable data of the sealing gasket to clarify the primary and secondary influences of the parameters of the skeleton on the structural strength. Through the regression equation, the minimum deformation size combination is optimized, and simulation reproduction is carried out to verify the calculation accuracy. Then, the feasibility of the compression resilience simulation verification scheme is established.

The material properties of the flexible graphite and TC4 titanium alloy are shown in Table 1. The influences of the skeleton thickness t, arc radius R, wave tooth depth h, and wave tooth spacing P on the deformation of the sealing gasket are analyzed. The graphite plate and the metal skeleton are defined as bound contacts. Owing to the large number of convex arrays in the structure, the triangular mesh can characterize the boundary and surface morphology with higher precision when dealing with complex geometric shapes and fine local details. Moreover, it shows adaptive ability to diverse structural features. The triangular mesh is used to mesh the composite gasket model, as shown in Fig6a, and the contact position between the skeleton and the flexible graphite is refined, as shown in Fig6b, to improve the calculation accuracy. On the basis of the load transfer characteristics of the flange end face, the normal uniform load of the upper and lower plates of the sealing gasket is set to 40 MPa, and the uniform load of the internal rectangular and rounded areas is set to 31.5 MPa in the finite element model. Moreover, the full degree of freedom constraint boundary condition is applied to the four bolt holes, as shown in Fig6c. The deformation data under different structural parameters are obtained via simulation calculations.

Table 1. Material Property Parameters.

Material	Density, g·cm^{-3}	Tensile Strength, MPa	Poisson's Ratio	Elastic Modulus, GPa
TC4 Titanium Alloy [18]	4.4	1057	0.3	102
Flexible Graphite [19]	0.9	4.0	0.4	0.186

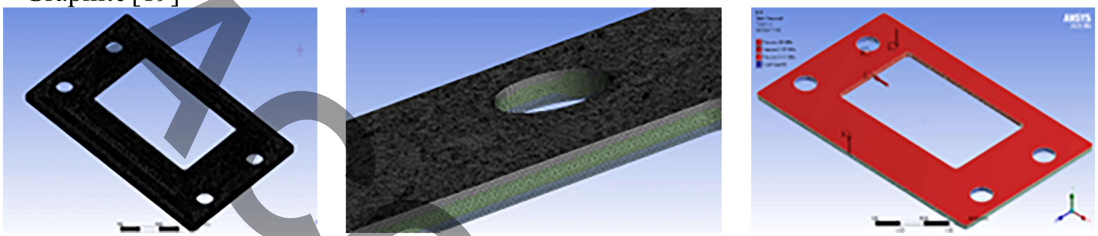

***a.** Mesh Subdivision* ***b.** Local Amplification* ***c.** Boundary Condition*

Figure 6. Establishment of the Finite Element Numerical Model.

On the basis of the limited requirements of the existing standards for the size of the gasket skeleton structure, combined with the engineering experience of the sealing element, four key geometric parameters that have a significant impact on the performance of the gasket structure are selected as the optimization variable data: skeleton thickness (t), arc radius (R), wave tooth depth (h) and wave tooth spacing (P), as shown in Table 2.

Table 2. Structural parameter level.

Factor	Skeleton Thickness t, mm	Arc Radius R, mm	Wave Tooth Depth h, mm	Wave Tooth Spacing P, mm
1	2.5	2.5	0.5	2.0
2	3.0	3.0	0.8	3.0
3	3.5	3.5	1.0	4.0

On the basis of multifactor optimization theory, the $L_{27}(3)^4$ orthogonal test design was used to construct the parameter combination matrix. The design method reduces the 81 theoretical combinations of the four-factor, three-level system to 27 typical schemes through the principle of orthogonality. Under the premise of ensuring the decoupling between factors, uniform coverage of the test space is realized, and the influence degree of each parameter on the deformation index is systematically evaluated to ensure that the optimal parameter combination is obtained under limited computing resources. Fig7. Deformation results shows the stress–strain field distributions of the third group, the 15th group, and the 22nd group of sealing gaskets in Table 3. The numerical simulation results reveal that under the action of a medium pressure load, the maximum deformation occurs in the narrow and long side areas of the sealing surface, which is obviously different from other areas. This phenomenon of deformation concentration is closely related to the geometric structure of the narrow and long edge regions. Owing to the relatively narrow geometric structure, the moment of inertia of the section decreases when subjected to high-pressure stress, which induces local deformation. In contrast, the nonnarrow edge region shows good deformation coordination because of its good structural continuity.

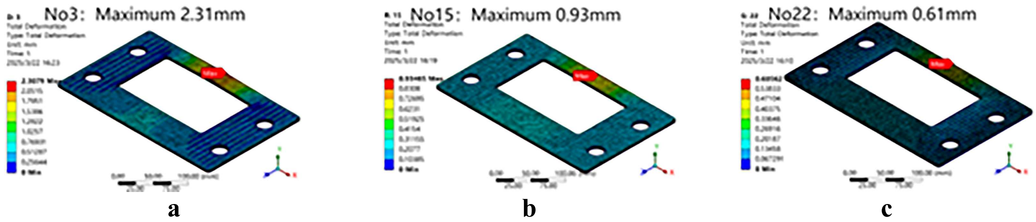

Figure 7. Deformation results.

Table 3 shows the structural parameter combinations of 27 sets of orthogonal tests and the corresponding maximum deformation μ values. Quantitative analysis reveals that the skeleton thickness t has a dominant effect on deformation suppression: when t is 3.5 mm, the average deformation is 60.8% lower than that when t = 2.5 mm. The group number 22 (t3R2h1P1) obtained the minimum deformation μ = 0.61 mm under the optimal parameter combination, whereas the group number 3 (t1R1h3P3) obtained a deformation of 2.31 mm due to the thinnest skeleton thickness (t=2.5 mm), which was 3.79 times the optimal value. The wave tooth spacing parameter shows a double effect at P = 2.0 mm. When coupled with a larger skeleton thickness ($t \geqslant$ 3.0 mm), the deformation decreases (such as group numbers 16 and 22), but when combined with a thinner skeleton (t=2.5 mm), the deformation increases (group number 1). This phenomenon indicates that there is an interaction between the parameters.

Table 3. Simulation Results.

number	Skeleton Thickness t, mm	Arc Radius R, mm	Wave Tooth Depth h ,mm	Wave Tooth Spacing P, mm	Largest Variable μ, mm
1	2.5	2.5	0.5	2.0	1.21
2	2.5	2.5	0.8	3.0	1.53
3	2.5	2.5	1.0	4.0	2.31
4	2.5	3.0	0.5	3.0	1.70
5	2.5	3.0	0.8	4.0	1.93
6	2.5	3.0	1.0	2.0	1.31
7	2.5	3.5	0.5	4.0	1.98
8	2.5	3.5	0.8	2.0	1.53
9	2.5	3.5	1.0	3.0	1.77
10	3.0	2.5	0.5	3.0	0.97
11	3.0	2.5	0.8	4.0	1.21
12	3.0	2.5	1.0	2.0	0.83
13	3.0	3.0	0.5	4.0	1.12
14	3.0	3.0	0.8	2.0	0.80
15	3.0	3.0	1.0	3.0	0.94
16	3.0	3.5	0.5	2.0	0.76
17	3.0	3.5	0.8	3.0	0.92
18	3.0	3.5	1.0	4.0	1.07
19	3.5	2.5	0.5	4.0	0.85
20	3.5	2.5	0.8	2.0	0.63
21	3.5	2.5	1.0	3.0	0.76
22	3.5	3.0	0.5	2.0	0.61
23	3.5	3.0	0.8	3.0	0.71
24	3.5	3.0	1.0	4.0	0.83
25	3.5	2.5	0.5	2.0	0.77
26	3.5	3.5	0.8	4.0	0.79
27	3.5	3.5	1.0	3.0	0.70

On the basis of the data obtained from the orthogonal experimental design method, a multiple linear regression (MLR) model was constructed for parameter analysis. The deformation prediction model is shown in Formula (7) [20]:

$$Y = b_0 + b_1 X_1 + \ldots + b_p X_p + e \tag{7}$$

The design matrix **X** and the response vector **Y** are defined as follows:

$$\mathbf{X} = \begin{pmatrix} 1 & t_1 & R_1 & h_1 & P_1 \\ 1 & t_2 & R_2 & h_2 & P_2 \\ \vdots & \vdots & \vdots & \vdots & \vdots \\ 1 & t_{27} & R_{27} & h_{27} & P_{27} \end{pmatrix}, Y = \begin{pmatrix} \mu_1 \\ \mu_2 \\ \vdots \\ \mu_{27} \end{pmatrix} \tag{8}$$

The least-square principle is used to solve the regression coefficient vector $\boldsymbol{b}$.

$$\hat{\mathbf{b}} = (X^T X)^{-1} X^T y \tag{9}$$

Where $\boldsymbol{X^T X}$ and $\boldsymbol{X^T y}$ can be calculated via Formulas (10) and (11), respectively:

$$\mathbf{X^T X} = \begin{pmatrix} 27 & \sum_{i=1}^{27} t_1 & \sum_{i=1}^{27} R_i & \sum_{i=1}^{27} h_i & \sum_{i=1}^{27} P_i \\ \sum_{i=1}^{27} t_i & \sum_{i=1}^{27} t_i^2 & \sum_{i=1}^{27} t_i R_i & \sum_{i=1}^{27} t_i h_i & \sum_{i=1}^{27} t_i P_i \\ \sum_{i=1}^{27} R_i & \sum_{i=1}^{27} t_i R_i & \sum_{i=1}^{27} R_i^2 & \sum_{i=1}^{27} R_i h_i & \sum_{i=1}^{27} R_i P_i \\ \sum_{i=1}^{27} h_i & \sum_{i=1}^{27} t_i h_i & \sum_{i=1}^{27} R_i h_i & \sum_{i=1}^{27} h_i^2 & \sum_{i=1}^{27} h_i P_i \\ \sum_{i=1}^{27} P_i & \sum_{i=1}^{27} t_i p_i & \sum_{i=1}^{27} R_i P_i & \sum_{i=1}^{27} h_i P_i & \sum_{i=1}^{27} P_i^2 \end{pmatrix} \tag{10}$$

$$\mathbf{x^T y} = \begin{pmatrix} \sum_{i=1}^{27} \mu_i \\ \sum_{i=1}^{27} t_i \mu_i \\ \sum_{i=1}^{27} R_i \mu_i \\ \sum_{i=1}^{27} h_i \mu_i \\ \sum_{i=1}^{27} P_i \mu_i \end{pmatrix} \tag{11}$$

On the basis of the Python platform, the parameters, regression coefficients, and P values of the linear regression equation are calculated as shown in Table 4.

Finally, the regression equation of the quantitative relationship between the skeleton thickness (t), wave tooth radius (R), wave tooth depth (h), wave tooth spacing (P), and deformation (μ) structural parameters is established as shown in Formula (12):

$$\mu = 0.45 - 0.51t - 3.13R + 0.58h + 0.75P \tag{12}$$

Table 4. Linear Regression Results.

Parameter	Regression Coefficient	P
b_0	0.45	0.003
b_1	-0.51	0.001
b_2	-3.13	0.244
b_3	0.58	0.435
b_4	0.75	0.002

The regression coefficient showed that the parameters b_1 and b_2 were negatively correlated with b_0, and b_3 and b_4 was positively correlated with b_0. The p values of the parameter b_2 and b_3 corresponding to the wave tooth radius (R) and the wave tooth depth (h) are too large, indicating that the two are not significant enough. To further improve the regression equation and eliminate the insignificant variables R and h, the simplified model is constructed by considering the interaction effect between the skeleton thickness (t) and the wave tooth spacing (P), as shown in Equation (13):

$$\mu = b_0 + b_1 t + b_2 P + b_3 (t \times P) \tag{13}$$

L2 regularization is used to suppress the potential collinearity of parameters:

$$\hat{\mathbf{b}} = \arg\ \min \min_{b} \left(\| y - Xb \|^2 + \lambda \| b \|^2 \right) \tag{14}$$

The final nonlinear regression model for the deformation is Formula (15):

$$\mu = 0.38 - 0.47t + 0.68P + 0.05(t \times P) \tag{15}$$

The overall significance of the model was assessed via analysis of variance (ANOVA) [21]:

$$\begin{cases} SSR = \sum_{i=1}^{27} (\hat{y}_i - \bar{y})^2 \\ SSE = \sum_{i=1}^{27} (y_i - \hat{y}_i)^2 \\ SST = \sum_{i=1}^{27} (y_i - \bar{y})^2 \end{cases} \tag{16}$$

Calculate the statistic F and the coefficient of determination R^2:

$$\begin{cases} F = \dfrac{SSR/k}{SSE/(n-k=1)} \\ R^2 = 1 - \dfrac{SSE}{SST} \end{cases} \tag{17}$$

The results of the variance analysis show that the F statistic of the regression model reaches 18.76 (regression degree of freedom k = 4, residual degree of freedom df = 22). According to the statistical standard, the significance level α = 0.05 can be obtained from $F_\alpha \approx 2.82$. Because the F value is greater than the critical value, the established regression model is significant overall. The determination coefficient R^2 is 0.87, which confirms that the regression model can effectively explain 87% of the deformation variation and has high prediction accuracy and reliability.

On the basis of a comprehensive consideration of deformation and graphite indentation, the parameter combination t3R3h1P1 (skeleton thickness t = 3.5 mm, arc radius R = 3.5 mm, wave tooth depth h = 0.5 mm, wave tooth spacing P = 2.0 mm) is selected. While ensuring the strength requirements, the graphite layer and the metal skeleton have sufficient contact area.

3.3 Simulation Verification

For the optimal parameter combination t3R3h1P1 predicted by the nonlinear regression model of deformation, refined numerical verification is carried out to calculate the maximum deformation. Using the Ansys Workbench statics module, under the premise of maintaining the original boundary conditions, the multiscale meshing strategy is implemented to locally refine the skeleton–graphite contact interface.

The numerical verification test reveals that the maximum deformation of the gasket with the optimized parameter combination (t = 3.5 mm, R = 3.5 mm, h = 0.5 mm, P = 2.0 mm) is 0.54 mm, as shown in Fig8a. Normal Proportion. Compared with the optimal group of the orthogonal test (group number 22, maximum deformation of 0.61 mm), it is reduced by 11.5%, and the maximum deformation position is still concentrated in the narrow and long edge regions. The spatial consistency with the deformation position of the 27 groups of samples in the orthogonal test confirms the stability of the deformation mechanism. The prediction accuracy and engineering applicability of the regression equation for the deformation behavior of sealing gaskets are further verified. On the basis of the visual analysis requirements of finite element postprocessing, to clearly reveal the deformation gradient distribution characteristics of the sealing gasket, the deformation field of the sealing gasket is enhanced and expressed as shown in Fig8b. Deformation Amplification. The enlarged cloud image clearly reveals that the periodic triangular convex array and the flexible graphite layer form a multistage nested sealing interface, and the triangular convex array does not experience plastic deformation under a working load, which confirms the sealing integrity and mechanical strength of the structure under high-pressure conditions.

a. Normal Proportion *b. Deformation Amplification*

Figure 8. Deformation Results.

3.4 Compression rebound verification

To further verify the feasibility of the scheme t3R3h1P1, according to the national standard [22], the nonlinear structure module of ANSYS Workbench is used to study the compression–resilience characteristics. Maintaining the original meshing system, the load is implemented in three stages, as shown in Fig9. Compression Rebound Load Application Process. The lower plate surface of the gasket was fixed, and the upper plate surface was subjected to a uniform load linearly increasing from 0 MPa to 1.75 MPa at a rate of 0.5 MPa·s-1 during the pretightening stage. After 10 s, the initial compression was recorded, and the initial thickness of the gasket T_1 was calculated. The compression stage continues to load at the same rate to 35 MPa for 10 s to obtain and record the gasket compression ΔT_1; in the rebound stage, the uniform load is unloaded to 1.75 MPa at the same rate for 10 s to record the unrecovered compression ΔT_2. After the simulation, the obtained data are input into Formulas (5) and (6) to calculate and verify the compression and resilience of the sealing gasket.

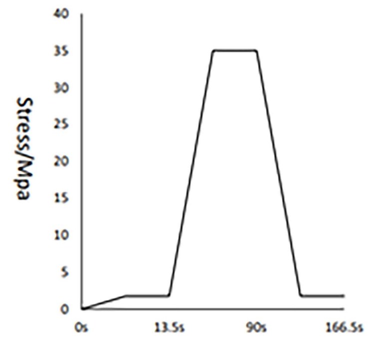

Figure 9. Compression Rebound Load Application Process.

The numerical simulation results of the test (Fig10. Compression Rebound Results) show that the gasket (Scheme t3R3h1P1) produces an elastic compression deformation of 0.21 mm in the initial pretightening stage, as shown in Fig10a. When the gasket is loaded to 35 MPa at a rate of 0.5 MPa·s^{-1} and held at 10, the total compression amount is 1.15 mm, as shown in Fig10b, and the compression amount of the gasket after the rebound stage is 0.14 mm, as shown in Fig10c. The calculation results show that the thickness T_1 of the gasket under the initial load is 4.79 mm. The compression amount ΔT_1 under the total load is 1.15 mm; the unrecovered compression amount ΔT_2 returned to the initial load is 0.14 mm. The overall deformation is average, and there is no large deformation in the region.

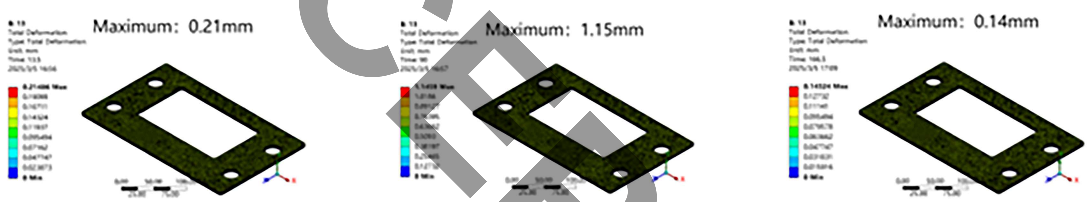

a b c

Figure 10. Compression Rebound Results.

The data are input into formulas 5 and 6 for calculation:

$$ompression\ ratio = \frac{1.15}{4.79} \times 100 = 24.0\%$$

$$rebound\ \text{ratio}(\%) = \frac{1.15 - 0.14}{1.15} = 87.8\%$$

Under the premise of ensuring the gasket strength requirements, the compression rate of the designed composite gasket is 24.0%, and the rebound rate is 87.8%, which meets the requirements of the national standard [23] for the compression rate and rebound rate of the sealing gasket. The final design of the sealing gasket skeleton size is as follows: skeleton thickness t = 3.5 mm, arc radius R = 3.5 mm, wave tooth depth h = 0.5 mm, and wave tooth spacing P = 2.0 mm.

4 Experimental Analysis

As flexible graphite is a typical anisotropic porous rheological material, evaluating the sealing performance of flexible graphite faces multiscale coupling challenges. Microscopically, the slip effect is dominated by van der Waals forces between the graphite flakes, and the porosity distribution jointly affects the compression rebound behavior. Macroscopically, the interface contact stress between the metal skeleton and the graphite layer exhibits significant nonlinear characteristics. In addition, the local stress concentration caused by the wave tooth structure is difficult to capture accurately via homogenization modeling [24],[25]. To verify the reliability of the designed nonstandard sealing gasket without considering leakage caused by molecular flow

[26], a hydrostatic pressure simulation experiment was used as a supplementary verification of the numerical simulation.

4.1 Experimental Scheme

In accordance with the API 6A-2021 standard [27], the main core components of the experimental equipment include a reaction device, a hydraulic control device, and a data acquisition device. A schematic diagram of the hydrostatic pressure experimental device is shown in Fig11.Hydrostatic pressure test schematic diagram. By manipulating the hydraulic control device to control the pressure, the condition of the sealing surface of the reaction device can be observed, and the pressure data can be recorded in real time by a data acquisition instrument.

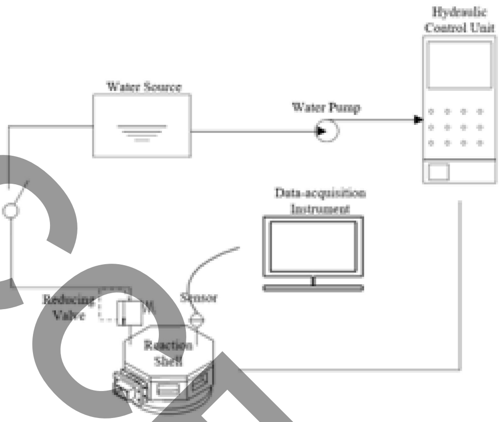

Figure 11. Hydrostatic pressure test schematic diagram.

The experimental process is shown in Fig12. Schematic diagram of the hydrostatic pressure experiment. The hydraulic control device achieves pressure control by adjusting the flow rate and internal pressure of the liquid. The core is composed of a high-precision proportional valve and a digital pressure controller, and the automatic pressure control device is shown in Fig13a. Internal Pressure Experimental Control Box. First, it was linearly pressurized to 31.5 MPa at a rate of 0.5 MPa·s-1, after which it entered the 3 min steady pressure stage. After the pressure relief stage is reduced to 0 MPa at the same rate, the secondary loading is immediately carried out to 31.5 MPa, and the secondary pressure is stabilized for 3 minutes to verify the creep recovery characteristics of the sealing interface. The reaction device platform is anchored to the laboratory seismic base by anchor bolts to ensure the stability of the system during loading. The sample is connected to the reaction shell by bolts, as shown in Fig13b. Specimen Load. The electronic monitoring panel HMI interface of the system supports real-time monitoring of the pressure–time curve to ensure the traceability of the experimental data. The timing is started when the equipment and pressure monitoring table are isolated from the pressure source and the outer surface of the body component is completely dry. After the completion of the experiment, the sample was disassembled to check whether cracks, plastic deformation, or a graphite layer peeling on the surface of the sample occurred.

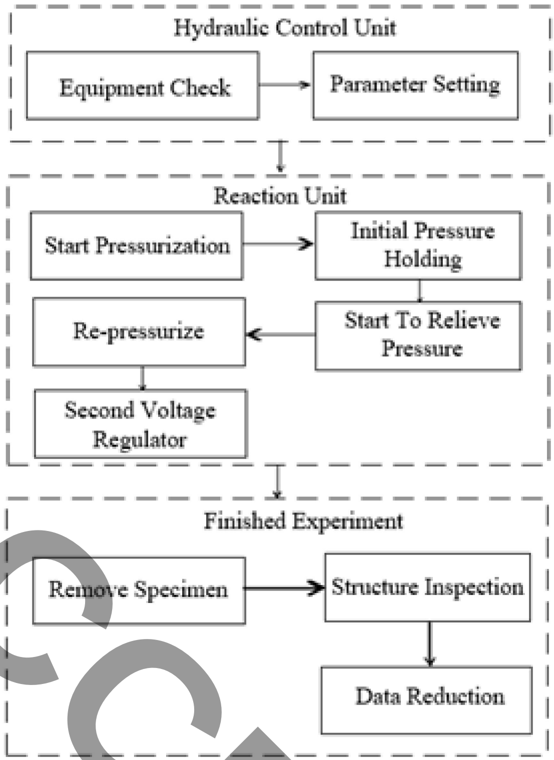

Figure 12. Schematic diagram of the hydrostatic pressure experiment.

***a.** Internal Pressure Experimental Control Box*

***b.** Specimen Load*

Figure 13. Part of the device is physical.

4.2 Test Sample

Through two sets of comparative tests, the sealing efficiency enhancement mechanism of the periodic triangular convex array and the engineering applicability of the orthogonal optimization design method are verified. Experimental group 1 was used as the reference control group, and a traditional nonstandard sealing gasket was used. Experimental group 2 is the optimization verification group. The periodic triangular convex array is embedded in the sealing skeleton, and the skeleton structure parameters are optimized via the $L_{27}(3)^4$ orthogonal experimental design method to prepare the improved gasket. The specific skeleton structure parameters are shown in Table 5.

Table 5. Skeleton Structure Parameters.

Group	Triangular Convex	Skeleton Thickness, mm	Arc Radius , mm	Wave Tooth Depth, mm	Wave Tooth Spacing, mm
1	-[a)]	3.5	3.5	0.5	2.0
2	+[b)]	3.5	3.5	0.5	2.0

[a)] means no; [b)] means exist.

4.3 Analysis of the effects

Although there was no obvious structural damage to the macroscopic morphology of the samples in the reference control group, there was little penetration leakage at the bolt–flange assembly interface when the pressure was increased to 20.9 MPa, and excessive penetration leakage occurred between the skeleton and the graphite layer when the pressure was further increased to 23.6 MPa. At this time, the seal has completely failed. When the bolt preload was increased to 120% of the design value, the leakage in the secondary pressure holding stage was slightly reduced, but it could still not meet the sealing needs. The pressure fluctuation curve of the experimental process is shown in Fig14. Experimental Group 1 Pressure fluctuation curves. The improved gasket of experimental group 2 exhibited breakthrough sealing performance under the same experimental conditions. There was no visible liquid leakage in the sealing sample during the whole experiment. The pressure–time curve of the hydrostatic experiment is shown in Fig15. Experimental Group 2 Pressure fluctuation curves. The maximum pressure during the experiment was 31.500 MPa, the minimum pressure was 0.007 MPa, the pressure fluctuation amplitude was always controlled within the allowable range, and the pressure of the sealing sample was stable during the two steady-state pressure holding stages.

Figure 14. Experimental Group 1 Pressure fluctuation curves.

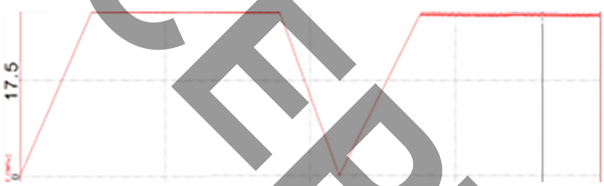

Figure 15. Experimental Group 2 Pressure fluctuation curves.

After the experiment, the device disassembled, and the surface deformation of specimen 1 is shown in Fig16a. The excessive bolt load led to lateral translation of the graphite layer and the skeleton, which led to overall sealing failure. This phenomenon reveals that the traditional sealing structure relies too much on the static contact stress caused by bolt preloading under dynamic loading, which makes it difficult to compensate for the sealing gap caused by the creep relaxation of the material and the interface percolation leakage between the skeleton and graphite. After the disassembly of specimen 2, the periodic triangular convex array on the surface of the metal skeleton was completely retained, and no microcracks were found in the wave tooth area. The graphite layer was closely combined with the skeleton interface, as shown in Fig16b. The experimental results show that the improved gasket effectively suppresses the problem of narrow edge deformation and interface failure, and its sealing performance and structural integrity are significantly better than those of traditional nonstandard gaskets, which meets the engineering requirements of extreme high-pressure conditions.

a b

Figure 16. Experimental Results.

5 Conclusion

(1) The mechanism of the influence of the structural parameters of the metal skeleton on the deformation of the sealing gasket is revealed on the basis of the regression equation of the quantitative relationship between the orthogonal method and the structural parameters. The results show that the thickness of the skeleton has the most significant effect on deformation, followed by the wave tooth spacing, and that the wave tooth depth and the arc radius have little effect.

(2) Based on the optimization, a nonlinear regression model of deformation is established. The optimal structural parameters of the gasket are 3.5 mm of skeleton thickness, 3.5 mm of arc radius, 0.5 mm of wave tooth depth, and 2.0 mm of wave tooth spacing. The ANSYS simulation shows that the gasket has a compression rate of 24.0% and a rebound rate of 87.9% while ensuring deformation, which meets the requirements of the national standard.

(3) The hydrostatic pressure experiment reveals that the new gasket proposed in this paper does not leak under a hydrostatic pressure of 31.5 MPa. The periodic triangular convex array tooth structure effectively suppresses interface failure and deformation and significantly improves the sealing reliability and structural strength under high-pressure conditions. Compared with traditional nonstandard gaskets, the proposed periodic triangular convex array structure has better sealing performance and structural integrity.

6 Compliance with Ethical Standards

There are no potential conflicts of interest in this document.
There are no human participants and/or animals studied in this document.
All authors are informed and agree.

References

[1] Z. Zhang, D. Wang, and Y. Guo, "Fretting friction and wear behaviors of spiral wound gasket (SWG) sealing surface," Tribology International, vol. 133, pp. 236–245, May 2019, doi: 10.1016/j.triboint.2019.01.017.

[2] M. Murali Krishna, M. S. Shunmugam, and N. Siva Prasad, "A study on the sealing performance of bolted flange joints with gaskets using finite element analysis," *International Journal of Pressure Vessels and Piping*, vol. 84, no. 6, pp. 349–357, Jun. 2007, doi: 10.1016/j.ijpvp.2007.02.001.

[3] D. J. Yang, B. Q. Gu, "Influence of Deformation Characteristics of Different Metal Framework on Mechanical Properties of Flexible Graphite Composite Gasket," *Journal of Nanjing University of Technology*, vol. 69, no. 4, pp. 105–109, Sep. 2017, doi: 10.3969/j.issn.1671-7627.2013.04.022.

[4] J. Liu, Q. Wang, "Failure Analysis and Improvement of Metal Skeleton of Flexible Graphite Corrugated Metal Gaskets for Valve," *Fluid Machinery*, vol. 41, no. 3, pp. 46-48, Mar. 2013, doi: 10.3969/j.issn.1005-0329.2013.03.010.

[5] Q. Chen, S. K. Gan, X. D. Liu, and Y. C. Liu, "Test Study on Structure and Technological Parameter Optimization of W-shaped Flexible Graphite Spiral Wound Gaskets" *Lubrication and Sealing*, vol. 39, no. 9, pp. 104-107, Sep. 2014, doi: 10.3969/j.issn.0254-0150.2014.09.022

[6] X. Yao, X. J. Wang, X. J. Liu, Z. M. Chen, and Z. R. Huang, "Friction-wear Properties and Mechanism of Hard Facing Pairs of SiC and WC," *Journal of Inorganic Materials*, vol. 34, p. 673, Jan. 2019, doi: 10.15541/jim20180435.

[7] W. Zheng, J. Sun, C. Ma, and Q. Yu, "Interface Leakage Theory of Mechanical Seals Considering Microscopic Forces," *Coatings*, vol. 13, no. 8, p. 1435, Aug. 2023, doi: 10.3390/coatings13081435.

[8] J. J. Sun, Q. G. Chen, and Z, B, Ji, "Interface Leakage Mechanism Analysis of Contact Mechanical Seal," *Journal of Chemical Industry*, vol. 69, no. 4, pp. 1528-1536, Sep. 2017, doi: 10.11949/j.issn.0438-1157.20170908.

[9] Q. Liu, Z. Wang, Y. Lou, and Z. Suo, "Elastic leak of a seal," *Extreme Mechanics Letters*, vol. 1, pp. 54–61, Dec. 2014, doi: 10.1016/j.eml.2014.10.001.

[10] L. Jiang, L. X. Fu, P. L. Zhang, Y. Zhang, M. D. Yu, and J. Tian, "Research on Calculation Method of Leakage Rate of Graphite Gasket Seal," *Nuclear Power Engineering*, vol. 44, pp. 141-147, Dec. 2022, doi: 10.13832/j.jnpe.2023.01.0141.

[11] D. D. L. Chung, “A review of exfoliated graphite,” *Journal of Materials Science*, vol. 51, pp. 554-568, Jul. 2015, doi: 10.1007/s10853-015-9284-6.
[12] E. Solfiti and F. Berto, “A review on thermophysical properties of flexible graphite,” *Procedia Structural Integrity*, vol. 26, pp. 187–198, Jan. 2020, doi: 10.1016/j.prostr.2020.06.022.
[13] P. Jaszak, R. Grzejda, J. Kluczyński, and P. Zmarzły, “Basic Design Parameters Influencing on Axial Stiffness of the Spiral Wound Gasket,” *Materials*, vol. 16, no. 18, Sep. 2023, doi: 10.3390/ma16186209.
[14] M. D. Li, Z. H. Duan, and X. Q. Qiu, “Test Study on Rebound Performance of Corrugated Tooth Composite Gasket under Normal Temperature Compression,” *Lubrication and Sealing*, vol. 34, pp. 91-93+109, Mar. 2009, doi: 10.3969/j.issn.0254-0150.2009.03.025.
[15] X. H. Jia, H. M. Chen, X. G. Li, and Y. M. Wang, “Mechanical Properties of Graphite Gasket Seal Interface,” *Journal of Tsinghua University (Natural Science Edition)*, vol. 56, pp. 167-170, Feb. 2016, doi: 10.16511/j.cnki.qhdxxb.2016.22.005.
[16] L. Wang, B. Wang, J. L. Xue, and J. H. Tao, “ Test and Comparison Study on Mechanical and Sealing Performance of Flexible Graphite Metallic Toothed Gasket and Spiral Wound Gasket,” *Pressure Vessel*, vol. 39, pp. 1-7, May. 2022, doi: 10.3969/j.issn.1001-4837.2022.05.001.
[17] L. Zhu, Y. Liu, M. Li, X. Lu, and X. Zhu, “Calculation Model of Mechanical and Sealing Properties of NiTi Alloy Corrugated Gaskets under Shape Memory Effect and Hyperelastic Coupling: I Mechanical Properties,” *Materials*, vol. 15, p. 4836, Jul. 2022, doi: 10.3390/ma15144836.
[18] S. Sun, D. X. E, “Time-Dependent Springback for TC4 Titanium Alloy at Room Temperature,” *Rare metal materials and engineering*, vol. 46, pp. 3267-3271, Nov. 2017.
[19] G. Mathan and N. Prasad, “Evaluation of effective material properties of spiral wound gasket through homogenization,” *International Journal of Pressure Vessels and Piping*, vol. 87, pp. 704–713, Dec. 2010, doi: 10.1016/j.ijpvp.2010.10.003.
[20] X. R. Chen, "*Probability Theory and Mathematical Statistics*," Science Press, Beijing, China, 2000.
[21] Y. Liu and G. Salvendy, “Effects of measurement errors on psychometric measurements in ergonomics studies: Implications for correlations, ANOVA, linear regression, factor analysis, and linear discriminant analysis,” *Ergonomics*, vol. 52, pp. 499–511, Apr. 2009, doi: 10.1080/00140130802392999.
[22] Standardization Administration of China, “GB/T 12622-2008 *Standard test method for compressibility and recovery of gaskets for pipe flanges*,” China Standards Press Beijing, China, 2008.
[23] Standardization Administration of China, “GB/T 19675.2-2023 *Reinforced flexible graphite gaskets for pipe flanges—Part 2: Class designated*,” China Standards Press, Beijing, China, 2023.
[24] E. Solfiti and F. Berto, “Mechanical properties of flexible graphite: review,” *Procedia Structural Integrity*, vol. 25, pp. 420–429, Jan. 2020, doi: 10.1016/j.prostr.2020.04.047.
[25] X. G. Li, M. X. Shen, C. L. Wang, S. J. Wei, J. Li, and X, D, Peng, “Sealing performance of flexible graphite corrugated metal composite gaskets,” *Journal of Chemical Industry*, vol. 66, pp. 1417-424, Dec, 2014, doi: 10.11949/j.issn.0438-1157.20141172.
[26] B. Gu, Y. Chen, and D. Zhu, “Prediction of Leakage Rates Through Sealing Connections with Nonmetallic Gaskets,” *Chinese Journal of Chemical Engineering*, vol. 15, pp. 837–841, Dec. 2007, doi: 10.1016/S1004-9541(08)60011-7.
[27] F. J. Schuh and T. R. Sampson, “API Offshore Standards Activities: Wellhead And Christmas Tree Equipment,” May 1986, doi: 10.4043/5240-MS.